

Evaluating Input Domain and Model Selection for Deep Network Ultrasound Beamforming

Jaime Tierney^{ID}, Adam Luchies^{ID}, Matthew Berger, and Brett Byram^{ID}, *Member, IEEE*

Abstract—Improving ultrasound B-mode image quality remains an important area of research. Recently, there has been increased interest in using deep neural networks (DNNs) to perform beamforming to improve image quality more efficiently. Several approaches have been proposed that use different representations of channel data for network processing, including a frequency-domain approach that we previously developed. We previously assumed that the frequency domain would be more robust to varying pulse shapes. However, frequency- and time-domain implementations have not been directly compared. In addition, because our approach operates on aperture domain data as an intermediate beamforming step, a discrepancy often exists between network performance and image quality on fully reconstructed images, making model selection challenging. Here, we perform a systematic comparison of frequency- and time-domain implementations. In addition, we propose a contrast-to-noise ratio (CNR)-based regularization to address previous challenges with model selection. Training channel data were generated from simulated anechoic cysts. Test channel data were generated from simulated anechoic cysts with and without varied pulse shapes, in addition to physical phantom and *in vivo* data. We demonstrate that simplified time-domain implementations are more robust than we previously assumed, especially when using phase-preserving data representations. Specifically, 0.39- and 0.36-dB median improvements in *in vivo* CNR compared to DAS were achieved with frequency- and time-domain implementations, respectively. We also demonstrate that CNR regularization improves the correlation between training validation loss and simulated CNR by 0.83 and between simulated and *in vivo* CNR by 0.35 compared to DNNs trained without CNR regularization.

Index Terms—Beamforming, contrast-to-noise ratio (CNR) regularization, deep learning, end-to-end training, input domain, ultrasound.

Manuscript received December 18, 2020; accepted March 2, 2021. Date of publication March 8, 2021; date of current version June 29, 2021. This work was supported in part by NIH under Grant S10OD016216-01 and Grant R01EB020040, in part by NSF under Grant IIS-1750994, and in part by the Data Science Institute, Vanderbilt University. (Corresponding author: Jaime Tierney.)

Jaime Tierney and Brett Byram are with the Department of Biomedical Engineering, Vanderbilt University, Nashville, TN 37235 USA (e-mail: jaime.e.tierney@vanderbilt.edu; brett.c.byram@vanderbilt.edu).

Adam Luchies is with the Department of Biomedical Engineering, Vanderbilt University, Nashville, TN 37235 USA, and also with Siemens Health Care, Issaquah, WA 98029 USA (e-mail: adam.c.luchies@vanderbilt.edu).

Matthew Berger is with the Department of Electrical Engineering and Computer Science, Vanderbilt University, Nashville, TN 37235 USA (e-mail: matthew.berger@vanderbilt.edu).

Digital Object Identifier 10.1109/TUFFC.2021.3064303

I. INTRODUCTION

ULTRASOUND B-mode imaging remains an invaluable tool for clinicians because it is real time, relatively affordable, and portable. However, poor image quality can make diagnostic and guidance tasks with ultrasound unreliable. This problem is particularly relevant for abdominal imaging applications for which deep penetration and high signal-to-noise ratio (SNR) are required but difficult to achieve when imaging through many tissue layers that cause reverberation and other sources of clutter [1].

To address sources of image degradation and improve image quality, many advanced beamforming methods have been proposed, including coherence-based techniques [2]–[4], adaptive apodization schemes [5]–[7], as well as model-based approaches [8]–[11]. Despite achieving image quality improvements compared to conventional delay-and-sum (DAS), most of these advanced methods have not been adopted clinically because they are computationally intensive, limited by user-defined parameters, or do not translate well to clinical application.

To address these limitations, based on the success of model-based beamforming, our group proposed the use of deep neural networks (DNNs) to accomplish the same task more efficiently [12]. In addition to our efforts, several other groups have proposed DNN approaches for improving ultrasound image quality. Generally, these efforts fall under one of the two classes. The first class uses conventional DAS or advanced beamformer output as ground truth target data. These efforts include DNNs that aim to reconstruct fully sampled data from some form of subsampled transmit events [13]–[21], DNNs that aim to reconstruct a conventional DAS image from raw channel data [22], and DNNs that aim to mimic advanced beamformer output [23], [24]. These approaches, although effective, are theoretically restricted in terms of image quality to the desired fully sampled DAS or advanced beamforming output. In contrast, the second class, under which our approach falls, includes DNNs that use physical ground-truth information as the target domain and are therefore theoretically capable of surpassing DAS or advanced beamformer performance. Among these efforts are DNNs that aim to simultaneously perform image enhancement and segmentation using ground-truth segmentation maps [25]–[27], DNNs that aim to reduce speckle using ground-truth echogenicity maps [28], and DNNs that aim to perform an aperture domain regression-based beamforming using ground-truth simulations [12], [29]–[31].

DNNs are a machine learning technique that work by applying successive transformations to an input in order to learn a desired output. Input values are passed through multiple “hidden” layers of artificial neurons, each with its own transformation weight and bias. Training involves minimizing the error between the transformed input and the desired output by repeatedly updating the transformation weights using gradient descent or similar. Neural networks have been shown to be universal approximators that can be trained to estimate any continuous function [32], and the depth of the network has been shown to be correlated with the complexity of the function being approximated [33]. Therefore, DNNs are highly applicable in the context of model-based beamforming, for which DNNs work by approximating the optimal nonlinear regression parameters for preserving the aperture domain signal of interest and suppressing sources of clutter. Apart from easing computational burden, trained DNNs are intended to be user independent, and thus, completely adaptive, allowing for the potential of superior performance to other advanced techniques, as we and others have demonstrated previously [12], [27]–[30].

Compared to most other DNN beamforming methods among the second class described above, which typically operate on some form of time-domain data [25]–[28], our proposed DNN implementation has so far operated on individual frequencies in the aperture domain. Although this approach involves training separate networks for each frequency in addition to including computationally expensive forward and inverse short-time Fourier transforms per channel, we assumed that compared to time-domain approaches, our frequency-domain implementation would be more robust to varying pulse shapes due to phenomena such as depth-dependent attenuation and mismatch between training and testing pulses. We demonstrated previously that our DNNs are robust to various forms of image degradation, including sound speed variation, phase aberration, and reverberation clutter [31]. However, DNNs in general have not been tested on varied pulse shapes nor have frequency- and time-domain implementations been directly compared.

Apart from the added architectural and computational complexity of using frequency-domain data, our original implementation otherwise used a straightforward regression approach to accomplish adaptive beamforming. Specifically, a standard loss was computed between regressed output and ground-truth simulation or physical phantom aperture domain signals for a single spatial location. Although effective at suppressing off-axis scattering, because these DNNs operate on aperture domain signals, image quality on fully reconstructed data is not always correlated with network performance. In addition, DNNs that produce optimal image quality on simulated or phantom data often do not correlate to optimal image quality *in vivo*. These discrepancies make model selection difficult. We previously demonstrated that image quality-related aperture domain coherence metrics can be incorporated into the loss function [34]. However, because this approach still operates on aperture domains signals, a discrepancy between network performance and the image quality metrics that we use for network evaluation can still persist.

To address these shortcomings, we first compare our established frequency-domain implementation to different time-domain implementations, namely baseband in-phase and quadrature (IQ), analytic IQ, and radio frequency (RF). Although other groups have developed and evaluated a variety of time-domain DNNs for ultrasound beamforming [22], [25]–[28], [35], [36], in this work, we use time-domain implementations adapted from our previously proposed frequency-domain approach to facilitate fair comparisons between data representations. To this end, for each data representation evaluated, we use fully connected DNNs that perform an aperture domain signal regression using ground-truth simulated data for training. Unlike our frequency-domain approach that uses a separate network per frequency, we implement the time-domain networks using a single depth as input and a single network model per beamformer. We also develop networks that take multiple frequencies or depths as input with the hypothesis that under ideal conditions (i.e., no sources of image degradation), and given the same amount of information, time- and frequency-domain networks should perform similarly. Using simulated anechoic cyst test data, we evaluate and compare robustness of each input domain implementation to varying pulse shapes not seen during training. We also compare how well each input domain is able to generalize to physical phantom and *in vivo* data.

In addition to evaluating input domain approaches, we also propose a contrast-to-noise ratio (CNR)-based regularization to improve model selection for *in vivo* beamforming. This training scheme can be classified as end-to-end because our final metric, i.e., CNR, is included in our loss function [37]. Using CNR-regularization, we seek to demonstrate that image quality improvements on simulated training data will be more correlated with improvements on *in vivo* test data, thereby improving model selection.

II. METHODS

We begin by summarizing the different signal processing steps required for each input domain type used in this work. We then describe details pertaining to the neural networks, including our CNR-based regularization. Next, we summarize the training data. Finally, we describe the various experiments performed to compare input domains and evaluate CNR-based regularization for improving model selection.

A. Input Domain Signal Processing

Conventional DAS, frequency-domain DNN, and three different time-domain DNN beamformers are compared. Conventional DAS beamforming applies focusing time delays to received channel data and then sums across the channel dimension to form an image, as shown by the black boxes and arrows in Fig. 1. DNN beamforming involves additional signal preprocessing and postprocessing steps, as shown by the orange boxes and arrows in Fig. 1.

Fig. 2 shows the differences between each DNN input domain type. The frequency-domain implementation uses a short-time Fourier transform (STFT) with an axial kernel (shown as a red box in Fig. 1) equal to one pulselength

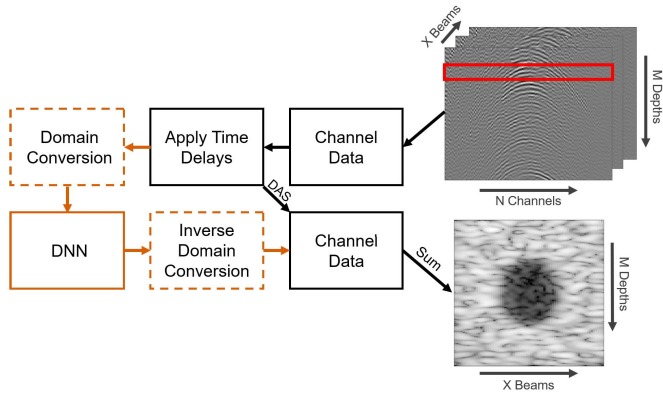


Fig. 1. Schematic summarizing DAS versus DNN ultrasound beamforming. Example channel data are depicted in the top right. An example axial kernel used in frequency-domain DNN beamforming is indicated by the red box. Conventional DAS is indicated by the black boxes and arrows. Additional steps for DNN beamforming are indicated by the orange boxes and arrows. The B-mode image in the bottom right shows an example simulated anechoic cyst.

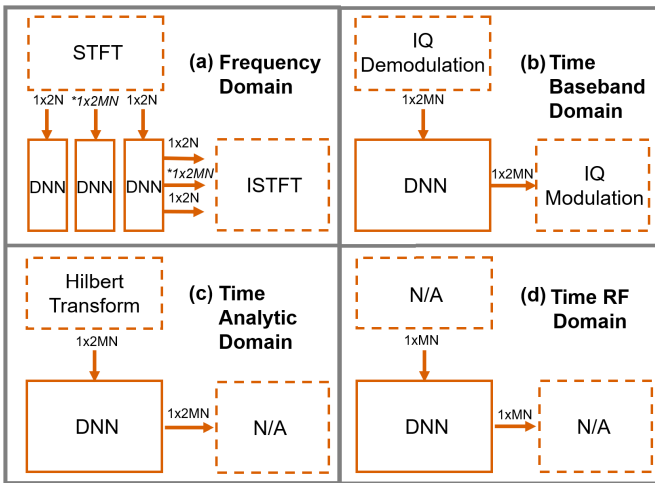


Fig. 2. Schematic highlighting the main differences between the input domain types used for DNN beamforming in this work. This figure indicates the immediate preprocessing and postprocessing steps relevant to the DNN regression. The input and output dimensions are indicated at each arrow with N and M representing the input channel dimension and number of signals used as input, respectively. *For the frequency-domain approach, for $M > 1$, only a single network was used. The factor of 2 for the frequency, and baseband IQ and analytic IQ input dimensions are for the real and imaginary components for a given input.

(16 samples for all data used in this work) and with a 90% axial kernel overlap. A separate network was used for each individual frequency within the pulse bandwidth. Three frequencies encompassed the bandwidth used for the established frequency-domain network beamformer, resulting in three networks per DNN beamformer, as shown in the top left of Fig. 2. The real and imaginary components for each frequency are stacked into a 1-D array, resulting in a $2N$ input dimension, where N is the number of channel elements. After being processed by the networks, the remaining frequencies are zero-padded and mirrored prior to performing an inverse STFT (ISTFT).

For the time-domain implementations, a single network was used to process all depths. For the baseband IQ implementation, a Hilbert transform is applied to the channel data prior

to demodulating to baseband. Similar to the frequency-domain implementation, the input to the network is the stacked real and imaginary components. After being processed by the network, the output baseband IQ data are modulated back to the transmit center frequency to ensure constant processing for every data type. Although possible and practical for future adaptations, the demodulated baseband IQ data were not downsampled in this work to maintain a consistent sampling frequency for all implementations. For the analytic IQ domain approach, a Hilbert transform is applied to the data and the resulting real and imaginary components are stacked and used as input to the network. No postprocessing is required for the analytic IQ data. For the RF implementation, preprocessing and postprocessing are not required. The RF implementation does not include an imaginary component, and therefore, the input to the network is half the size of the other input domain approaches.

Because the frequency-domain network beamformers only process a certain bandwidth within a given STFT window, an inherent bandpass filtering is incorporated. To facilitate a fair comparison to DAS and the time-domain approaches, unless otherwise stated, all time-domain channel data are bandpass filtered prior to being processed by a DNN or summed for DAS. The bandpass filter was designed to preserve the same bandwidth as the frequency-domain data, but was applied to the full depth range as opposed to individual STFT windows.

In addition to the implicit bandpass filter, the frequency-domain approach also differs from the time-domain implementation because it incorporates a dimensionality reduction. In other words, the three most prominent frequency bins used for DNN processing encompass the majority of the information from the 16-sample STFT window, whereas the time-domain implementations use information from a single depth sample. To facilitate a fair comparison, multiple frequency and depth implementations were explored. For this approach, multiple frequencies or depths were used as input to a single DNN beamformer, resulting in a single network architecture for all input domain implementations. Input sizes of 3 and 16 axial signals were implemented and compared. An input size of three axial signals is considered because three frequencies encompassed the bandwidth of interest for the established frequency-domain beamformers. An input size of 16 axial signals is considered because the full axial STFT kernel used in this work is 16 depth samples (i.e., 16 frequency bins). Therefore, the networks with an input size of 16 axial signals will have equivalent information among input domains, apart from not including imaginary components with the RF approach. For the networks with an input size of 16 axial signals, no bandpass filtering was incorporated before or after DNN beamforming. For both multi-input networks, the real frequency or depth samples are stacked and then concatenated with the imaginary samples to achieve a $1 \times 2MN$ input dimension ($1 \times MN$ for the RF implementation), where M is the number of axial signals. Apart from the factor of M included in the input and output dimensions, the multi-input network beamforming approach differs from the schematic in Fig. 2 only in that the frequency

domain no longer uses a multinet implementation but rather mimics the time-domain single network architectures. To be clear, a 16-sample window was still used for all STFT implementations. For the single-input STFT approach, three separate networks were trained for each of the three most prominent frequency bins within the 16-sample window. For the multi-input approaches, the most prominent 3 or all 16 frequency bins within the 16-sample window were stacked into a single vector for network processing.

For all input domain approaches, only the real signal output from the networks was used for final evaluation. The same envelope detection scheme was applied to all real-valued output signals to ensure a 90° phase-shifted imaginary component.

B. Neural Networks

To be consistent with the known signal coherence patterns of ultrasound channel data [38], our networks are fully connected across the transducer elements. However, both the time- and frequency-domain implementations are implicitly convolutional through depth and across beams. This is intuitive for the time-domain approaches for which the same set of network weights are applied to all depths and beams. For the frequency-domain approach, the same sets of network weights are applied to the same frequency bins within each STFT window through depth and for each beam.

All networks in this work were created and trained using Pytorch [39] and are feed-forward, fully connected, and multilayered. All training was performed on GPUs provided by the Advanced Computing Center for Research and Education (ACCRES), Vanderbilt University, Nashville, TN, USA. All networks used a rectified linear unit (ReLU) activation function [40] and a variant of stochastic gradient descent called Adam [41]. For the Adam optimizer, parameter values matched those suggested by Kingma and Ba [41] (i.e., $\alpha = 10^{-3}$, $\beta_1 = 0.9$, and $\beta_2 = 0.999$). Each aperture domain input signal was normalized to a maximum of 1 prior to being processed by the network. Network weights were initialized using a zero mean Gaussian random variable with variance equal to $((2/n))^{1/2}$, where n is the size of the previous layer [42], [43]. A patience of 20 epochs was used to determine model convergence based on validation loss improvement.

Thirty three sets of hyperparameters were randomly chosen from the values in Table I. To ensure that differences are not due to different hyperparameters, the same hyperparameters were used to train 33 networks for each input domain approach for each single and multi-input implementation (i.e., 396 DNN beamformers total). Although the hyperparameters were the same, the starting weights were different and the preprocessing and postprocessing were different between the different input approaches, as described in Section II-A.

C. CNR-Based Regularization

To compute CNR during training, multiple regressed output spatial locations need to be reconstructed to compute the mean and variance in specified regions of interest. This is complicated for our original frequency-domain approach because

TABLE I
HYPERPARAMETER SEARCH SPACE

Hyperparameter	Values
Batch Size	10-1000
Number of Hidden Layers	1-7
Layer Width	520-1040
Input Gaussian Noise	True or False
Input Dropout Probability	0-0.5
Hidden Node Dropout Probability	0-0.5
Batch Norm	True or False
Loss Function	L1, L2, Smooth L1
Weight Decay	0, 0.0001, 0.001

each frequency bin is trained separately and also an ISTFT needs to be performed in order to compute CNR. Therefore, although not impossible with a frequency-domain implementation, based on results from the input domain evaluation, CNR-based regularization was developed and evaluated using the time-domain analytic IQ data only.

To incorporate CNR into the loss function during training, each mini-batch must contain samples within regions of interest from a single training data realization. Therefore, for all CNR-regularized networks, the batch size was set to the number of training examples taken from each training data realization, which equates to a batch size of 5,946. The same 33 sets of hyperparameters were used to train networks with and without CNR-regularization, resulting in an additional 66 networks. The only difference between the networks without CNR regularization and the time analytic networks from Section II-B is the fixed larger batch size. These additional networks without CNR-regularization were trained to allow for CNR to be computed during training on the validation data (described in Section II-D).

For each mini batch, the aperture domain examples were normalized prior to being passed through the network. The stacked real and imaginary output data from the network were then unnormalized, combined into analytic data, and summed across the aperture domain. The magnitude was taken to compute the envelope of each signal. CNR was then computed on the envelope data for which specified background and lesion examples (see Fig. 3) were used to compute CNR as follows:

$$\text{CNR} = 20 \log_{10} \frac{|\mu_{\text{background}} - \mu_{\text{lesion}}|}{\sqrt{\sigma_{\text{background}}^2 + \sigma_{\text{lesion}}^2}} \quad (1)$$

where μ and σ are the mean and standard deviation of the uncompressed envelope, respectively. As described in Section II-D, training data were made from simulated anechoic cysts that have a theoretical CNR of 5.6 dB [44]. Therefore, a CNR loss was computed as follows:

$$L_{\text{CNR}} = \lambda ||\text{CNR}_{\text{out}} - 5.6||_l \quad (2)$$

where λ is a scaling term, CNR_{out} is the estimated CNR on the output data from the model, and l represents the loss function used for that network, i.e., L1, L2, or Smooth L1. A fixed λ value of 0.005 was used for the model selection study. A range of λ values between 0.0005 and 10 were also evaluated using

TABLE II
TRAINING DATA ACQUISITION SUMMARY

Parameter	Value
Transmit frequency	5.208MHz
Pitch	298 μ m
Sampling Frequency	20.832MHz
Number of Elements	65
Number of Beams	69
Focus	7cm
Simulation Decimation Factor	25
Bandwidth	60%

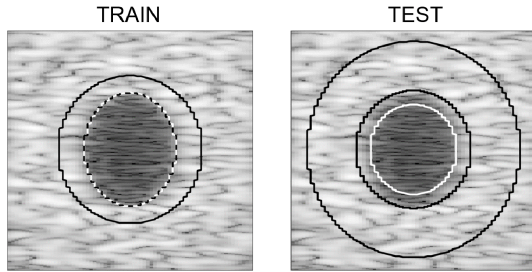


Fig. 3. Boundaries of background and lesion regions of interest are indicated in black and white, respectively, for training (left) and for computing image quality on test data (right). For CNR regularization, the training regions of interest were used to compute CNR during training.

the selected model. The above CNR loss function is then added to the standard data fidelity loss function L_F computed on the regressed output signals compared to the target signals as follows:

$$L = L_F + L_{\text{CNR}}. \quad (3)$$

D. Training Data

Training data for all networks evaluated in this work were generated from 24 simulated 5-mm-diameter anechoic cyst realizations within a 1 cm \times 1 cm area of tissue scatterers, as shown in the bottom right of Fig. 1. Using Field II [45], focused channel data were simulated using the acquisition parameters indicated in Table II. The center of the cyst was located at the transmit focus. Background tissue scatterer realizations were generated to ensure 12 scatterers per resolution cell. Channel data were simulated using a 25 \times sampling rate and then downsampled. No noise was added to any channel data prior to training. Gaussian noise added during training was used as a hyperparameter, as shown in Table I and described in Section II-B.

Training data for the input domain comparison study were split into either accept or reject regions depending on whether the aperture signal within the STFT kernel originated from a location outside or inside of the cyst, respectively. Accept and reject regions for training data are shown in Fig. 3. If the center point of the STFT kernel was primarily outside of the cyst, it was considered the accept region data. If the center point of the STFT kernel was primarily inside of the cyst, it was considered the reject region data. For the accept region data, the network was trained to preserve the input signal.

For the reject region data, the network was trained to zero out the input signal. The number of accept and reject training examples was made equal (i.e., the full background was not used for training). Although the time-domain implementations do not require an axial kernel, the same selection criteria based on the STFT kernel was used for the time-domain approaches to ensure the number and spatial location of the training examples matched between input domains. For the time-domain data, the center depth within the STFT kernel was used as the training example.

Training data for the CNR-regularization study were generated similarly as for the input comparison study. However, because only the time analytic IQ input domain approach was considered and also to improve sampling of the regions of interest used to compute CNR, each pixel within the accept and reject regions was used for training (as opposed to the center depth within each STFT window).

Of the 24 training realizations, for both the input comparison and CNR-regularization studies, 20 realizations were used for training and the remaining four were used for validation. For the input domain comparison study, a total of 55 640 training examples and 11 128 validation examples were used for training each network. For the CNR-regularization study, a total of 109 920 training examples and 21 984 validation examples were used for training each network.

E. Experiments

Experiments were designed with the following two main questions in mind: 1) does there exist a superior data representation for training and testing DNNs for ultrasound beamforming? and 2) does the proposed CNR regularization improve model selection for *in vivo* beamforming? Table III summarizes the experiments for each of these two main objectives. This section is organized by each experiment and provides further detail on the data used to test the various hypotheses.

1) *Input Domain Comparison—Model Evaluation and Selection*: The purpose of this experiment was to perform a fair model evaluation and selection for each of the input domains and input sizes evaluated (i.e., 12 total). For each input domain, one input size and associated model were selected for further experimentation. The other main objective of this experiment was to test the hypothesis that frequency- and time-domain implementations should be equivalent when using an input size of 16 because the same amount of information is included.

To accomplish these pursuits, as described in Section II-B, a model search across 33 sets of hyperparameters was performed for each input domain and input size evaluated (i.e., 396 DNN beamformers total). Each model was trained with the data described in Section II-D. Each model was evaluated with a separate simulated anechoic cyst test set. Using the same geometry and acquisition parameters as described in Section II-D and Table II, 21 anechoic cyst channel data realizations were simulated for testing. Noise was added to each test example and was scaled to be 50 dB lower than the tissue signal. A single model and input size for each of the four

TABLE III
SUMMARY OF EXPERIMENTS. ALL DNNs USED IN THESE EXPERIMENTS WERE TRAINED WITH SIMULATED ANECHOIC CYSTS

Experiment	Objective	Summary
1	Input Domain Comparison	Evaluate and select models
2	Input Domain Comparison	Evaluate whether selected models can generalize to pulse shapes not seen during training
3	Input Domain Comparison	Evaluate whether selected models can generalize to physical phantom data
4	Input Domain Comparison	Evaluate whether selected models can generalize to <i>in vivo</i> liver data
5	CNR Regularization	Evaluate and select CNR-regularized models
6	CNR Regularization	Evaluate whether selected CNR-regularized models can generalize to <i>in vivo</i> liver data

data representations was selected based on CNR performance on the test data.

2) *Input Domain Comparison—Generalization to Varied Simulated Pulse Shapes*: The purpose of this experiment was to evaluate the robustness of the selected network for each of the four input domains on unanticipated varying pulse shapes not seen during training. Therefore, the hypothesis for this study is that DNN performance should be best at the training data pulse shape parameters and begin to degrade when the test pulse varies substantially from the training pulse.

Simulated anechoic cysts with no noise were created for this study using the same scatterer geometry, as described in Section II-D. No bandpass filtering was incorporated for any input domain type. This means that the frequency-domain beamformer used networks for each nonnegative frequency within the STFT window.

Three pulse shape parameters were investigated: center frequency, percent bandwidth, and ring-down effects. Apart from these parameters, acquisition settings matched those in Table II. To ensure that differences are not due to unresolved speckle, for the varied center frequency and percent bandwidth studies, the five scatterer realizations were generated to ensure 50 scatterers per resolution cell for the highest frequency and percent bandwidths evaluated. The sampling frequency fulfills the Nyquist criteria for the highest center frequency tested and therefore remained fixed at 20.832 MHz for all cases.

When varying each parameter, the other two parameters remained fixed at default values of 5.208 MHz center frequency, 60% bandwidth, and no ring down. The center frequency was varied between 3.208 and 7.208 MHz spaced by 100 kHz. Bandwidth percentages ranged from 20 to 80 spaced by 10. Ring-down percentages were implemented using the asymmetric Gaussian chirp model proposed by Demirli and Saniie [46]

$$s(t) = A(t - \tau) \cos(2\pi f_c(t - \tau) + \psi(t - \tau)^2 + \phi) \quad (4)$$

where $A(t) = \beta \exp(-\alpha(1 - r \tanh(mt))t^2)$. We used the suggested parameters for chirp rate ($\psi = -1$), phase ($\phi = 0$) and amplitude ($\beta = 1$). We set our center frequency (f_c) to 5.208 MHz, decay rate (α) to 30 s^{-2} , arrival time (τ) to zero, and then varied the coefficient controlling the degree of envelope asymmetry r between 0 and 0.9. An example pulse echo using $r = 0.9$ with substantial ring-down effect is shown in Fig. 4.

3) *Input Domain Comparison—Generalization to Physical Phantom Data*: Physical phantom data were used to evaluate the ability of the selected network for each of the four input

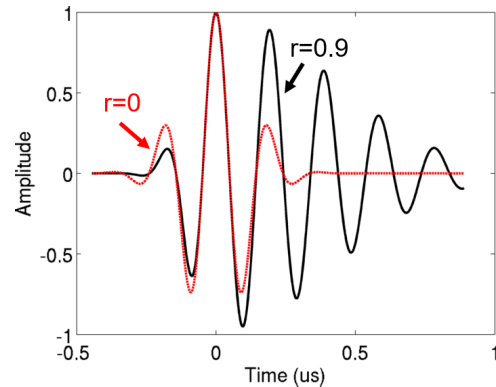


Fig. 4. Example pulse echoes with no ring down ($r = 0$) and with substantial ring down ($r = 0.9$) are shown in red and black, respectively.

domains to generalize to nonsimulated anechoic cyst data. Channel data were acquired of a quality assurance phantom (CIRS Model 040 GSE, Norfolk, VA, USA) using a Verasonics Vantage Ultrasound System (Verasonics, Inc., Kirkland, WA, USA) and ATL L7-4 (38 mm) linear array transducer. To ensure different speckle realizations, the probe was shifted in the elevation dimension to acquire ten different realizations each of a 5-mm and 10-mm-diameter cyst. The cysts were centered at about a 7-cm depth and 128 transmit beams were acquired. Acquisition parameters otherwise matched those in Table II.

4) *Input Domain Comparison—Generalization to In Vivo Data*: *In vivo* liver data were used to evaluate the ability of the selected network for each of the four input domains to generalize to nonsimulated and nonanechoic cyst data. In addition, to demonstrate the challenges with model selection and generalization to *in vivo* data, all 33 models for each of the four input domains were used to beamform the liver data. For each input domain, the model that produced the highest *in vivo* CNR was chosen as the “best” model. The best models were then compared to the selected models.

Informed written consent in accordance with Vanderbilt University’s institutional review board was given by a healthy 37-year-old male to acquire ultrasound images of his liver. Channel data were acquired using a Verasonics Vantage Ultrasound System (Verasonics, Inc., Kirkland, WA, USA) and ATL L7-4 (38 mm) linear array transducer. Fifteen different fields of view were acquired using 128 transmit beams. Acquisition parameters otherwise matched those in Table II.

5) *CNR Regularization—Model Evaluation and Selection*: The CNR regularization scheme was developed to address

two problems. First, because our networks operate on aperture domain data to perform an intermediate beamforming step, low training validation loss does not always correlate to high CNR on fully reconstructed images. Second, because ground-truth physical information is unknown *in vivo*, we use simulated data for training, which can result in a discrepancy between simulated and *in vivo* performance. Therefore, our hypotheses for this study are as follows. CNR regularization will result in higher negative correlation between simulated training validation loss and CNR computed on simulated training validation data (i.e., low validation loss will correlate to high CNR) and higher positive correlation between CNR computed on simulated training validation data and CNR computed on *in vivo* test data (i.e., high simulated CNR will correlate to high *in vivo* CNR).

To test these hypotheses, a model search across 33 sets of hyperparameters was performed for DNNs implemented with and without CNR regularization. Each model was trained with the data described in Section II-D. Training validation loss and the corresponding CNR computed on the simulated anechoic cyst training validation set ($n = 4$) were evaluated for each model. In addition, each model was used to beamform the *in vivo* test data described in Section II-E4 to evaluate the corresponding simulation and *in vivo* CNR performances.

For each case (i.e., with and without CNR regularization), one model was selected based on CNR performance on the simulated anechoic cyst training validation set. Using the selected CNR-regularized DNN, a range of λ scaling terms between 0.0005 and 10 were evaluated, as also described in Section II-C.

6) *CNR Regularization—Generalization to In vivo Data*: The *in vivo* test data described in Section II-E4 were used to further evaluate the ability of the selected DNNs with and without CNR regularization to generalize to *in vivo* data. Specifically, image quality performance was assessed qualitatively as well as quantitatively using CNR as well as image quality metrics other than CNR.

F. Image Quality Metrics

In addition to CNR (1), the following image quality metrics were used to evaluate beamformer performance for all of the generalization experiments in this work:

$$CR = -20 \log_{10} \frac{\mu_{\text{lesion}}}{\mu_{\text{background}}} \quad (5)$$

$$SNR_s = \frac{\mu_{\text{background}}}{\sigma_{\text{background}}} \quad (6)$$

$$GCNR = 1 - \int \min\{p_{\text{lesion}}(x), p_{\text{background}}(x)\} dx \quad (7)$$

where μ , σ , and p are the mean, standard deviation, and empirical density function [47] of the uncompressed envelope, respectively. Background and lesion regions of interest for the simulated training and test data are shown in Fig. 3.

III. RESULTS

The results are organized by the two main contributions of this work: 1) input domain evaluation and 2) image

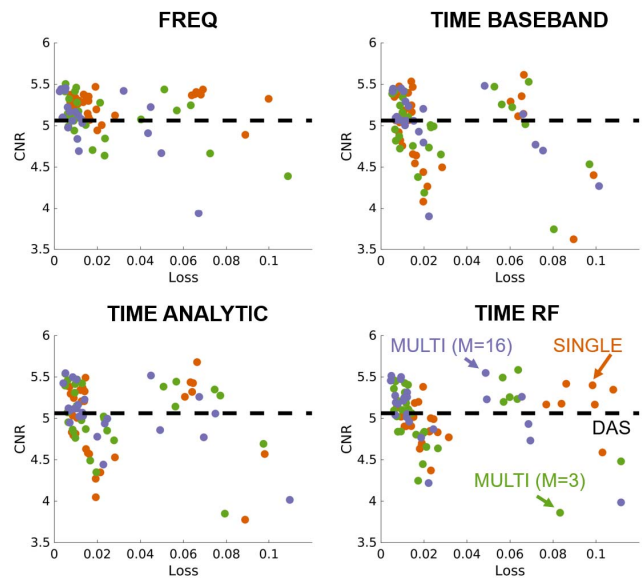


Fig. 5. Quantitative results are shown for experiment 1 (i.e., input domain DNN model evaluation). Average ($n = 21$) CNR versus validation loss is shown for each DNN beamformer (i.e., each dot) used to evaluate the simulated 50-dB SNR anechoic cyst test data. A separate plot is displayed for each domain type. Single-input and multi-inputs of 3 and 16 are displayed as the orange, green, and purple dots, respectively. DAS average CNR is indicated by the black dashed line in each plot.

quality-based regularization for improved model selection. The results are further organized by the experiments described in Section II-E and Table III.

A. Input Domain Comparison: Model Evaluation and Selection

1) *Model Evaluation*: Fig. 5 shows three things: 1) frequency-domain DNNs are more robust to varying network hyperparameters than time-domain DNNs; 2) time-domain DNNs are able to achieve comparable CNR to frequency-domain DNNs; and 3) larger input size does not translate to higher CNR. Compared to the time-domain DNNs, more of the frequency-domain DNNs produce CNR that is higher than that produced by DAS, suggesting that the frequency-domain DNNs are more robust to varying hyperparameters. However, time-domain DNNs overall produce as high if not higher CNR than frequency-domain DNNs. Finally, for all domain types, increasing the input size appears to enable lower training validation losses, but, apart from the time RF DNNs, increasing the input size does not seem to translate to higher CNR. It is noteworthy that the single depth RF DNNs are consistently worse than the single depth IQ DNNs, suggesting that phase is an important feature. We hypothesize that incorporating multiple depths into the time RF implementation effectively incorporates phase into the DNN.

It is also worth noting that the multiple-input approaches resulted in more outlier networks that did not train (i.e., validation loss remained constant). In addition, among the networks that take multiple-input depths simultaneously, the frequency-domain approaches resulted in more outliers

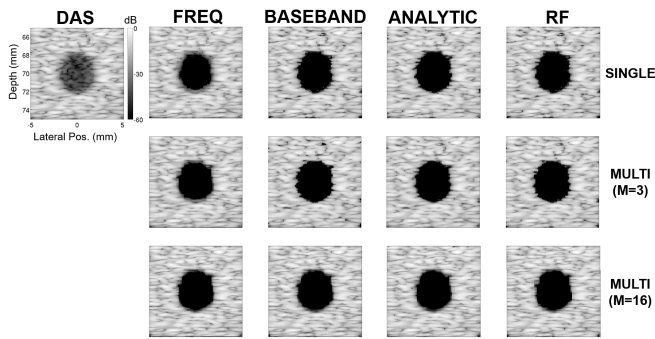


Fig. 6. Qualitative results are shown for experiment 1 (i.e., input domain DNN model evaluation). B-mode images of an example simulated anechoic cyst realization with 50-dB SNR beamformed using DAS (top left) and DNNs for each domain type (columns) and input size (rows). For each DNN case, the beamformer that produced the highest average CNR was used to make the B-mode image. Images are scaled to individual maximums and a 60-dB dynamic range.

than the time-domain approaches. Of the 33 networks trained for each input and domain type, a minimum of 2 were deemed outliers for all single-input cases, while a maximum of 11 were deemed outliers for the frequency-domain multiple-input approach with an input size of 16 axial signals.

The benefits of increasing the input size are more apparent qualitatively, as shown in Fig. 6. For the example shown in Fig. 6, for the time-domain data, the cyst edges and background speckle get progressively smoother as the input size is increased. For the frequency-domain data, the cyst appears to get progressively wider, indicating better lateral resolution, as the input size is increased. In addition, the images produced with networks that use an input size of 16 axial signals appear to converge to a common result. As hypothesized in Sections I and II-E1, this is expected given that the networks are given the same information from relatively clean data, albeit in a different format.

2) *Model Selection*: The network models with hyperparameters shown in Table IV produced the highest and second highest average CNR for the time- and frequency-domain single-input network beamformers, respectively, when tested on the simulated anechoic cyst data with 50-dB SNR. Therefore, the four models with these hyperparameters were used for all subsequent input domain comparison studies. Although a different set of hyperparameters produced the highest CNR for the established frequency-domain beamformer, the improvement was only by 0.03 dB (5.47 versus 5.44 dB), as shown in Fig. 5. Therefore, because this difference in CNR performance is so small, the frequency-domain beamformer that produced the second highest CNR was used for subsequent evaluation to ensure that differences between input domain types are not due to different hyperparameters.

B. Input Domain Comparison: Generalization to Varied Pulse Shapes

The hypothesis for this experiment was that DNN performance should be best at the training data pulse shape parameters and begin to degrade when the test pulse varies

TABLE IV
OPTIMAL HYPERPARAMETERS BASED ON CNR COMPUTED ON SIMULATED ANECHOIC CYST TEST DATA WITH 50-DB SNR

Hyperparameter	Value
Batch Size	745
Number of Hidden Layers	4
Layer Width	784
Input Gaussian Noise	True
Input Dropout Probability	0.3
Hidden Node Dropout Probability	0.2
Batch Norm	False
Loss Function	L1
Weight Decay	0

substantially from the training pulse. As shown in Fig. 7, this was not always the case. However, Fig. 7 shows that both frequency- and time-domain DNN approaches are robust to varying pulse shapes due to changes in transmit frequency, bandwidth, and ring-down effects and consistently produce higher image quality metrics compared to DAS.

For the varying transmit frequency analysis, DAS and all DNN approaches resulted in increased CNR, CR, and GCNR as the transmit frequency increased. This is noteworthy since the networks were trained on data that used a 5.208-MHz center frequency, suggesting that our hypothesis is not true for higher imaging frequencies. These image quality improvements are supported in Fig. 8, which shows example B-mode images made from data acquired at 3.208 and 7.208 MHz.

For the varying bandwidth analysis, DNN CNR decreased when the bandwidth deviated from the training bandwidth of 60%, as shown in Fig. 7. DAS image quality decreases for larger bandwidths, which is unexpected because increasing bandwidth should theoretically result in better resolution and, thus, image quality. DNN CR and GCNR also decrease as a function of increasing bandwidth, which also goes against our hypothesis. This trend is likely due to increased sidelobe levels, a trend similarly seen with resolution enhancing apodization [7]. In addition, this trend is qualitatively supported in Fig. 8, which shows example B-mode images made from data with transmit bandwidths of 40% and 80%. Based on these images, although expected resolution benefits are apparent for all beamformers for 80% bandwidth, the DNN cyst boundaries are less defined at the higher bandwidth, which supports the decreased CR and GCNR values with increasing bandwidth shown in Fig. 7. As for DAS, Fig. 8 shows how the resolution is better using an 80% bandwidth, but this also results in more refined speckle within the cyst, which is likely why CNR, CR, and GCNR decrease for DAS.

As hypothesized, increasing ring-down effects results in more variable image quality metrics, but overall the DNN beamformers are robust to these effects and consistently produce higher image quality than DAS, as shown in Fig. 7. Fig. 8 shows how increasing the ring down also results in decreased speckle resolution.

Overall, the baseband and analytic IQ implementations are more robust to varying pulse shapes than the other methods, as shown by the consistently higher metrics in Fig. 7.

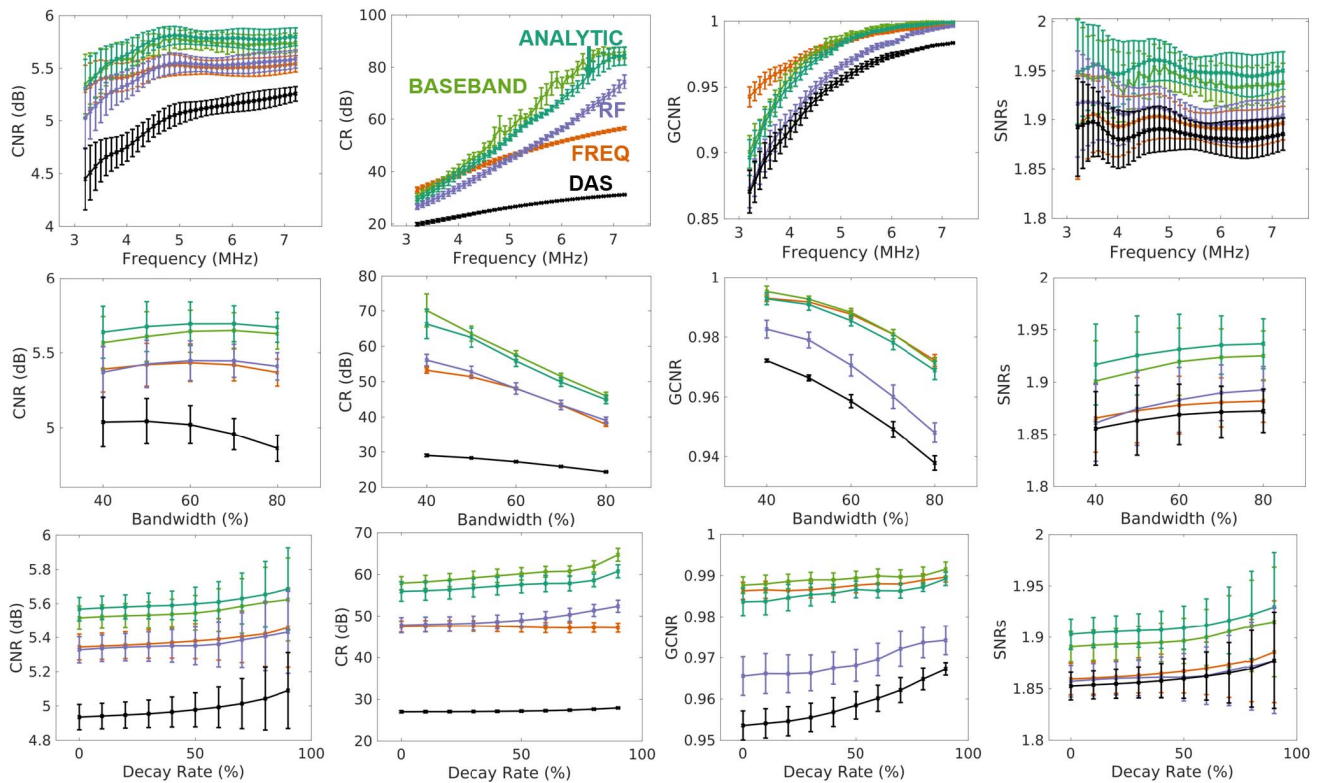


Fig. 7. Quantitative results are shown for experiment 2 (i.e., input domain generalization to varied pulse shapes). Average ($n = 5$) image quality metrics computed on simulated anechoic cyst test data as a function of varied transmit frequency (top), fractional bandwidth (middle), and ring-down decay rate (bottom). When varying each parameter, the other two parameters remained fixed at default values of 5.208-MHz center frequency, 60% bandwidth, and no ring down. Frequency, baseband IQ, analytic IQ, and RF are shown in orange, green, teal, and purple, respectively. DAS is indicated in black and error bars represent the standard deviation. For each DNN case, the beamformer that used hyperparameters indicated in [Table IV](#) was used for producing the data in these plots.

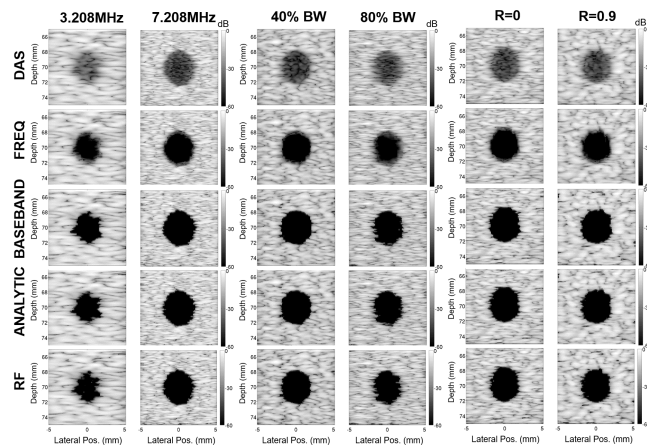


Fig. 8. Qualitative results are shown for experiment 2 (i.e., input domain generalization to varied pulse shapes). B-mode images of an example simulated anechoic cyst with different transmit frequencies (left), pulse bandwidths (middle), and ring-down effects (right) beamformed using DAS (top row) and DNNs for each domain type. For each DNN case, the beamformer that used hyperparameters indicated in [Table IV](#) was used to make each image. Images are scaled to individual maximums and a 60-dB dynamic range.

C. Input Domain Comparison: Generalization to Physical Phantom Data

Fig. 9 shows that the time-domain DNNs are able to generalize to physical phantom data and produce similar image

quality compared to the frequency-domain DNNs. **Fig. 9** shows box plots for which the median value for each method is the central mark in each box. The 25th and 75th percentiles are the bottom and top edges of each box, respectively. The bars extending from each box indicate the minimums and maximums, and outliers are marked in red. All DNN approaches produce higher CNR, CR, and GCNR compared to DAS. These results are qualitatively supported in [Fig. 10](#), which shows example B-mode images for each beamformer and physical phantom cyst size. For the examples in [Fig. 10](#), cyst visibility is clearly improved with the DNN approaches, but speckle quality does appear to degrade away from the cysts both axially and laterally for all cases.

D. Input Domain Comparison: Generalization to In vivo Data

Figs. 11 and **12** show that, similar to the physical phantom data, the time-domain DNNs are able to generalize to *in vivo* liver data and are able to produce similar image quality compared to the frequency-domain DNNs. **Fig. 11** shows the box plots for which the median value for each method is the central mark in each box. The 25th and 75th percentiles are the bottom and top edges of each box, respectively. The bars extending from each box indicate the minimums and maximums, and outliers are marked in red. These results further support that the time-domain implementations are

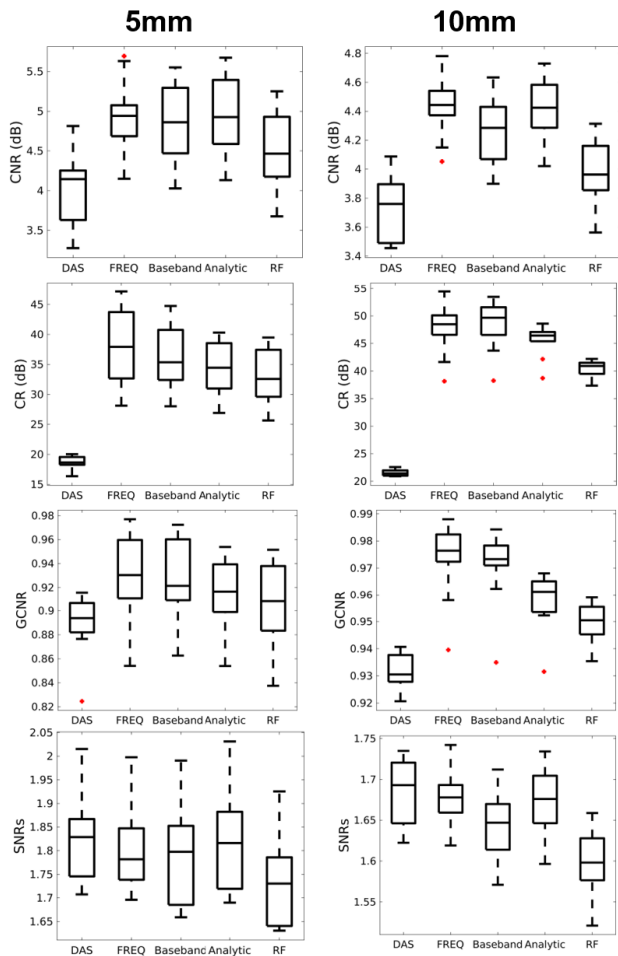


Fig. 9. Quantitative results are shown for experiment 3 (i.e., input domain generalization to physical phantom data). Box plots display image quality metrics for each domain type for the 5-mm (left) and 10-mm (right) diameter cyst physical phantoms. For each DNN case, the beamformer that used hyperparameters shown in Table IV was used for producing the data in these plots.

generally robust. However, unlike the above experiments, none of the DNN approaches are able to achieve CNR or SNRs improvements *in vivo* compared to DAS when using the selected models with hyperparameters shown in Table IV. This result is supported qualitatively in the top row of Fig. 12. CR improvements are apparent in these images compared to DAS for each DNN beamformer, but speckle dropout is also prevalent, resulting in low CNR and SNRs. Although the selected models perform poorly on *in vivo* data, other models were able to outperform DAS, as shown quantitatively in the right column of Fig. 11 and qualitatively in the bottom row of Fig. 12. This suggests that the problem with generalization to *in vivo* data is how models are selected as opposed to general DNN performance. Although it is possible to exhaustively test each model on *in vivo* test data, it is impractical and generally poor practice. Therefore, a better *in vivo* model selection approach is necessary.

E. CNR Regularization: Model Evaluation and Selection

The model hyperparameters selected for the above experiments produced beamformers that perform well for simulated

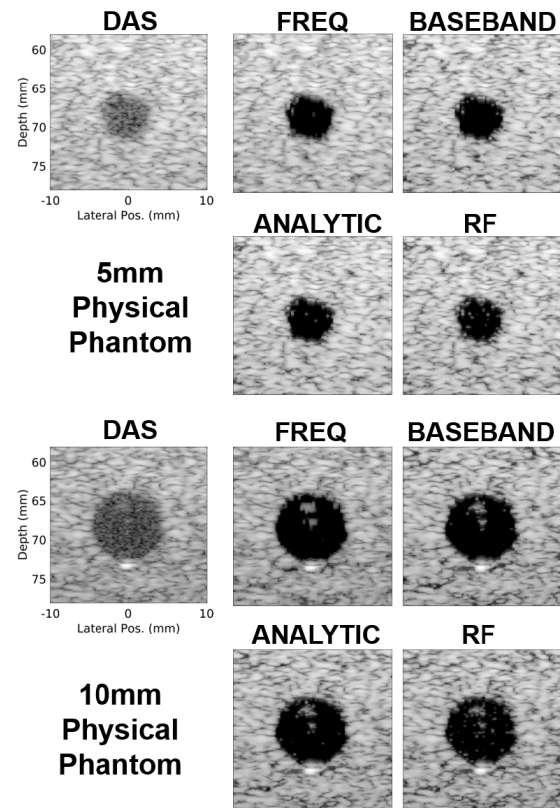


Fig. 10. Qualitative results are shown for experiment 3 (i.e., input domain generalization to physical phantom data). B-mode images of example 5-mm (top) and 10-mm (bottom) cyst physical phantom realizations beamformed using DAS and DNNs for each domain type. For each DNN case, the beamformer that used hyperparameters indicated in Table IV was used to make each image. All images are scaled to individual maximums and a 60-dB dynamic range.

and physical phantom anechoic cysts. However, when generalizing to a more variable *in vivo* field of view, those beamformers do not perform as well in terms of CNR and SNRs, as shown in Figs. 11 and 12. Despite this discrepancy, the time-domain approaches, especially the time analytic, consistently perform similar to the frequency-domain DNNs. Based on this result in addition to the simplified network architecture, the time analytic approach was used to further explore improvements in model selection using CNR regularization.

The teal dots in Fig. 13(a) and (b) represent different time analytic beamformers without CNR regularization and demonstrate the decorrelation between training validation loss and simulation CNR and training simulation CNR and *in vivo* test CNR, respectively. Based on these plots, CNR improvements compared to DAS are achieved with the time analytic DNN beamformers without CNR regularization. However, the beamformer that produces the highest simulated training CNR counter-intuitively has one of the highest training validation losses and also produces low *in vivo* CNR. When using the original model selection approach based on simulated CNR, the hyperparameters for the selected model without CNR regularization are the same as those in Table IV with the exception of the batch size that was set to 5496 for this study. Because of the different batch size and also the random initialized weights

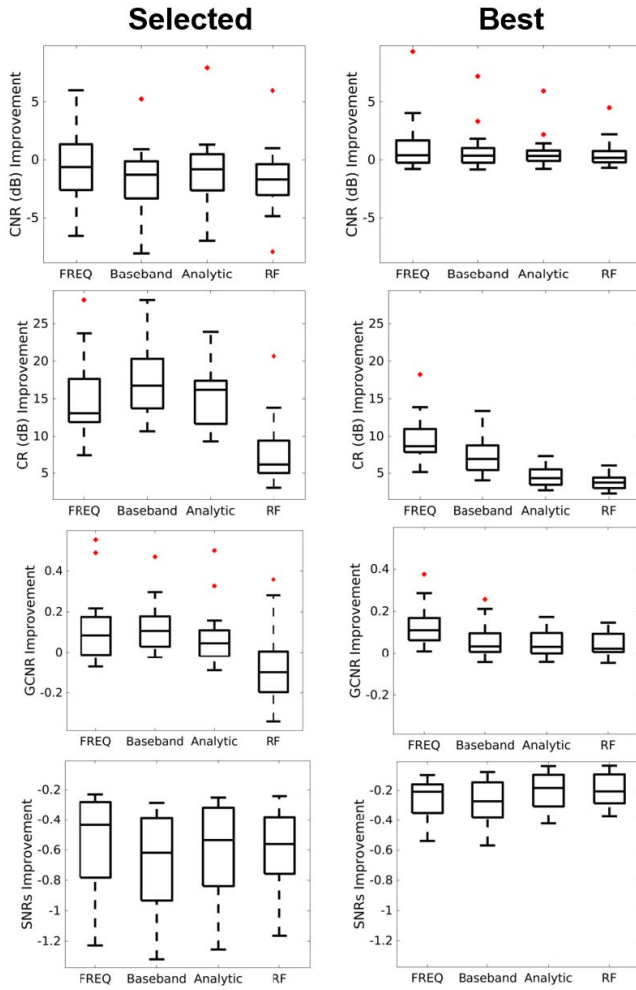


Fig. 11. Quantitative results are shown for experiment 4 (i.e., input domain generalization to *in vivo* data). Box plots display image quality improvements compared to DAS for each domain type computed on *in vivo* liver data. Results are shown for the selected DNN models with hyperparameters indicated in Table IV (left) and the models that produced best possible CNR for each case (right).

for training the separate networks, the image quality metrics are different than those reported in Section III-D for the time analytic *in vivo* data. In addition, because of the different regions of interest used to compute CNR during training, as shown in Fig. 3, the simulated CNR values are also different than the simulated CNR values reported in Section III-A.

In contrast to the data without CNR regularization, CNR-regularized DNNs address the discrepancy in model selection, as shown by the pink dots in Fig. 13(a) and (b) that represent different time analytic beamformers with CNR regularization. Based on these results, when CNR regularization is used, the model selected based on simulated CNR also converged to low training validation loss and produced high CNR *in vivo*. The selected CNR-regularized DNN hyperparameters are indicated in Table V. Overall, CNR regularization resulted in correlation values of -0.73 between training validation loss and simulated CNR and 0.07 between simulated and *in vivo* CNR, compared to 0.10 and -0.28 , respectively, without CNR regularization. These results are consistent with our two

TABLE V

OPTIMAL HYPERPARAMETERS BASED ON SIMULATED ANECHOIC CYST TRAINING CNR FOR CNR REGULARIZED DNN BEAMFORMING

Hyperparameter	Value
Batch Size	5496
Number of Hidden Layers	6
Layer Width	638
Input Gaussian Noise	False
Input Dropout Probability	0.3
Hidden Node Dropout Probability	0.2
Batch Norm	True
Loss Function	L2
Weight Decay	0

hypotheses for this experiment: CNR regularization resulted in higher negative correlation between training validation loss and simulated CNR and higher positive correlation between simulated and *in vivo* CNR.

Apart from better model correlation, CNR regularization noticeably improves simulated CNR, as shown by the separation between teal and pink dots in Fig. 13(a) and (b). Training progression of validation loss and simulated validation CNR is also shown for the selected models in Fig. 13(c) and (d), respectively. These plots demonstrate that the CNR-regularized DNN beamformers produce similar loss curves to the DNN beamformer without CNR regularization while also converging to a higher CNR.

Finally, Fig. 13(e) shows that the λ value used to regularize the CNR loss function can be adjusted to achieve higher CNR on simulated validation training data for the selected CNR-DNN model. However, increasing λ to place more emphasis on the CNR loss function results in a substantial drop in CR.

F. CNR Regularization: Generalization to In Vivo Data

Fig. 14 shows the qualitative improvements in image quality when using DNN beamforming with CNR regularization compared to conventional DNN or DAS beamforming. Specifically, the CNR regularized DNN reduces the speckle dropout that is seen in the conventional DNN images while maintaining contrast improvements compared to DAS. This result is supported quantitatively for the examples in Fig. 14 as well as on average across the full *in vivo* test set ($n = 15$), as reported in Table VI. For the results shown in Fig. 14 and Table VI, the hyperparameters indicated in Tables IV and V were used to train the selected conventional DNN and CNR regularized DNN, respectively.

IV. DISCUSSION

The results in this work suggest that, although the frequency-domain implementations are generally superior, it is possible to simplify DNN architectures by using time-domain data and multiple-input formats without substantially hindering image quality improvements. This is important because it simplifies the training process that is relevant when implementing training improvements and advancements like the CNR regularization proposed in this work. In addition, the time-domain approaches require less computation

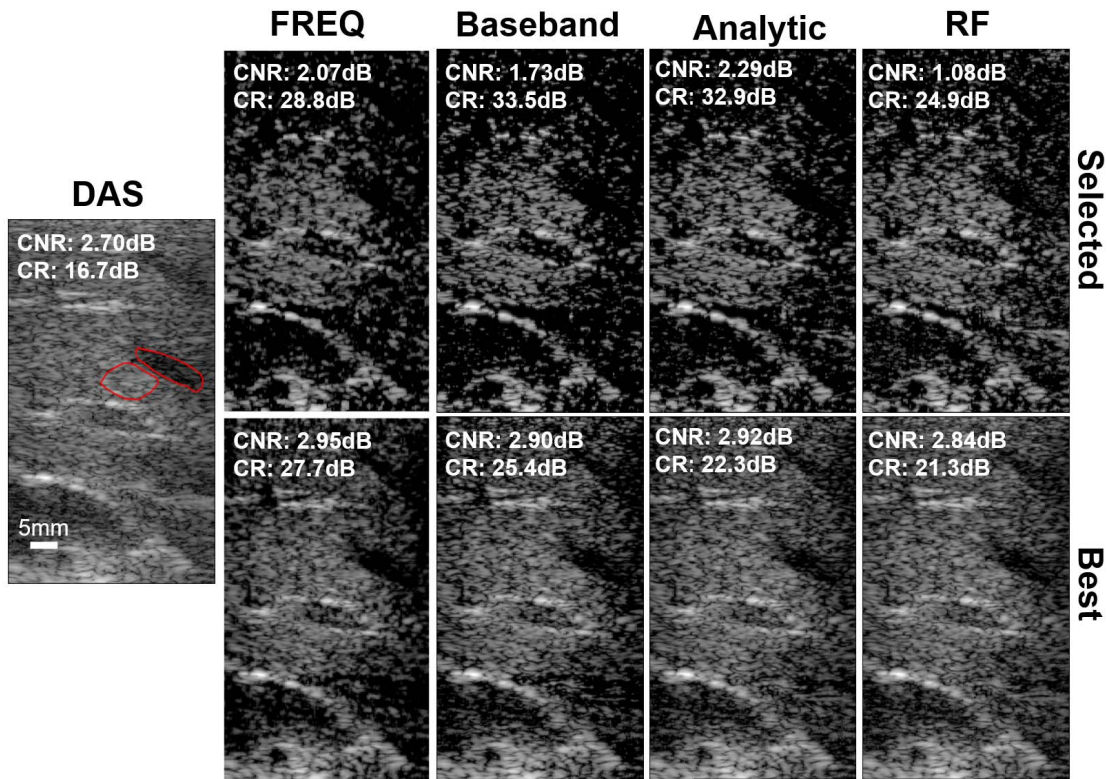


Fig. 12. Qualitative results are shown for experiment 4 (i.e., input domain generalization to *in vivo* data). B-mode images of an example *in vivo* liver realization beamformed using DAS, the selected DNN models (top) chosen as the models that produced the best CNR on simulated test data, and the best *in vivo* models that produced the highest *in vivo* CNR (bottom). For each selected DNN case (top), the beamformer that used hyperparameters indicated in Table IV was used to generate each B-mode image. Example regions of interest used to compute image quality metrics are displayed on the DAS image in red. CNR and CR values are indicated on each image. Images are scaled to individual maximums and a 60 dB dynamic range.

before and after network processing, which is ideal when pursuing real-time implementations. However, the traditional frequency-domain DNN approach generally outperformed the time-domain approaches when generalizing to the data least similar to the training data. For example, the frequency-domain DNNs produced the highest overall image quality metrics for the physical phantom data, as shown in Fig. 9. Having said that, the time-domain approaches, especially the baseband and analytic IQ, still outperformed DAS. Considering these conclusions, frequency-domain DNNs might be better suited when attempting to generalize to particularly noisy environments, while time-domain approaches are more practical for real-time or clinical applications.

For the analyses in this work, RF time-domain single-input DNN performance was consistently worse than the other time-domain single-input approaches. This suggests that phase is an important feature to include for DNN beamforming. Furthermore, the sample scheme that we used in this work makes it so that adjacent RF depths are about 90° out of phase. Therefore, the importance of phase information for DNN beamforming is also demonstrated by the improved image quality when multiple RF depths are used as input, as shown in Figs. 5 and 6.

Although sampling frequency was kept constant for the analyses in this work, it is worth noting that the baseband IQ data could be downsampled without changing

performance. Therefore, although the baseband IQ DNNs performed similar to the analytic IQ DNNs, the potential for improved computation time with the baseband IQ approach potentially makes it more practical for real-time implementations.

As indicated in the results, for the anechoic cyst evaluations, single-input models that were trained using the hyperparameters in Table IV produced consistently high CNR for all input domain types. However, when generalizing to *in vivo* data with several randomly placed cysts and structures, those hyperparameters did not produce the best performing DNNs. Similarly, when implementing the multi-input approaches, those hyperparameters were not optimal and actually were considered outliers for all of the multi-input cases with an input size of 16 axial signals. Also, as mentioned in Section III-A, the multi-input networks produced more outliers compared to the single-input networks, with the number of outliers increasing as the input size increased and with the most outliers (11 out of 33) occurring for the frequency-domain networks with an input size of 16 axial signals. This indicates that the multi-input approaches are more difficult to train, and future work will aim to investigate whether the hyperparameter space can be better adjusted for different input sizes. Having said that, a minimum success rate of 66% is not unreasonable and suggests that the hyperparameter space chosen is already generally robust.

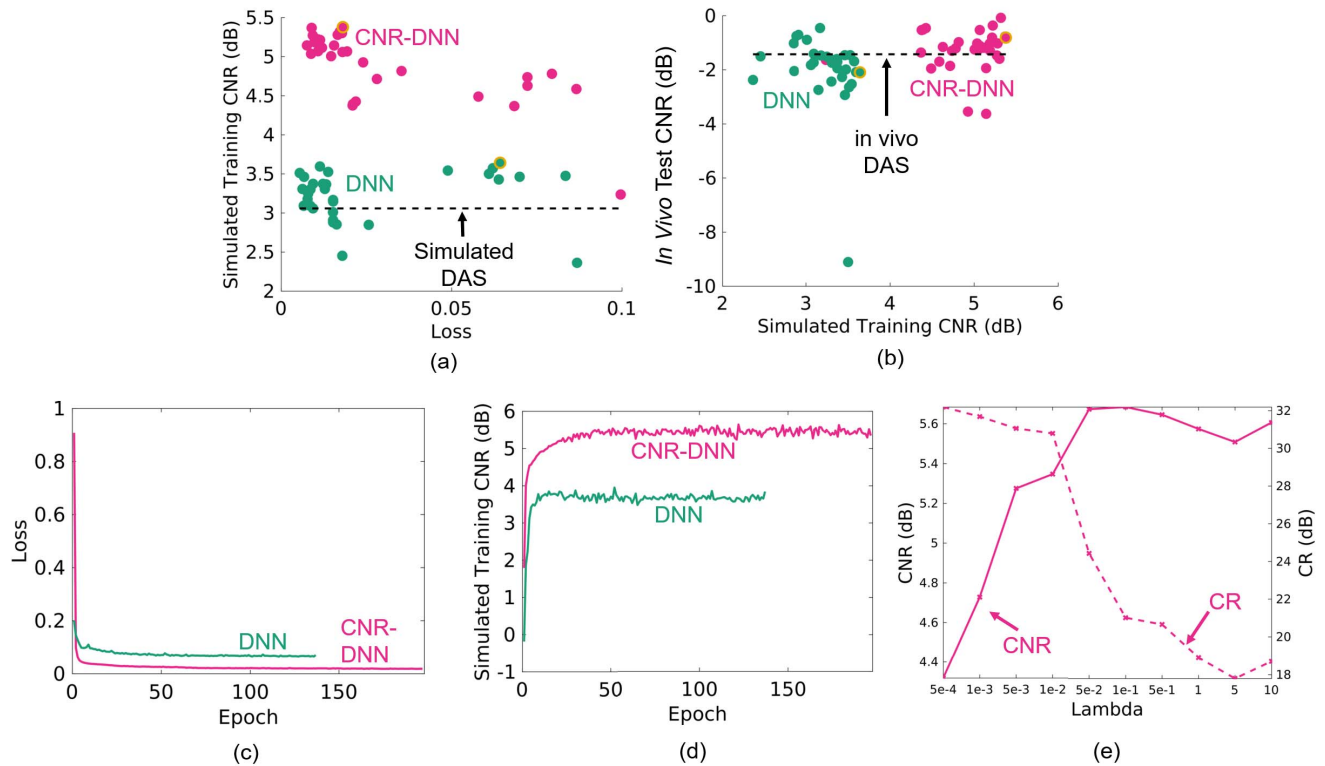


Fig. 13. Quantitative results are shown for experiment 5 (i.e., CNR regularization model evaluation and selection). (a) Average ($n = 4$) CNR computed on simulated training validation anechoic cyst data versus training validation loss is shown for each normal DNN beamformer (teal) and CNR-regularized DNN beamformer (pink). Average simulated DAS CNR is indicated by the black dashed line. (b) Average ($n = 4$) CNR computed on simulated training validation anechoic cyst data versus average CNR ($n = 15$) computed on *in vivo* test data is shown for each normal DNN beamformer (teal) and CNR-regularized beamformer (pink). Average *in vivo* DAS CNR is indicated by the black dashed line. Each dot in (a) and (b) represents a different set of hyperparameters used to train each model. The models chosen for each case (i.e., without and with CNR regularization) are indicated with gold outlines. Time analytic single-input approach was used for all of the beamformers in these plots. (c) Validation loss per epoch for the selected models is shown for DNN and CNR-DNN. (d) CNR computed on simulated validation training data is shown for each epoch for the selected models. (e) Average CNR and CR computed on simulated validation training data using the selected CNR-DNN model with different λ values.

The results in Section III-E show that CNR-regularization worked as a strategy for addressing the model selection problem and substantially improved the selected model performance for *in vivo* beamforming. It was reasonable to use the single-input time analytic approach for development of this training scheme because of the substantial evidence included in this work that this approach is generally robust. However, the time analytic approach is also easily implemented due to the minimal preprocessing and postprocessing steps, as shown in Fig. 2. However, it is possible to perform CNR regularization on the other input domain types or the multi-input approaches and these implementations should be considered for future work.

Simulated anechoic cysts were used for training and testing in this work because they provide intuitive and clean ground-truth information for training a DNN to successfully suppress off-axis scattering and generalize, as we have demonstrated previously for our frequency-domain approaches [29], [31]. In addition, training with anechoic cysts allowed us to incorporate a theoretical CNR value into our CNR regularization, which prevented overestimation of CNR. However, as exemplified in Fig. 13(e), training with anechoic cysts to suppress off-axis scattering results in an inherent bias toward CR when minimal weight is used for the CNR regularization.

Because of this tradeoff, in addition to CNR translating well to clinical observation [48], it made sense to use CNR for regularization in this work. However, it is plausible that the same tradeoff is not as apparent when training with, say, hypoechoic cysts and that regularizing with CR or GCNR is more effective. Therefore, it is worth investigating in future work if different types of training data and/or different regularization schemes improve network performance and model selection. As part of this work, it would also be interesting to see whether there is any benefit to incorporating a combination of image quality metrics into the loss function.

Although the presented results are specific to the fully connected architectures used in this work, we believe that there are several conclusions that are relevant for deep learning beamforming efforts in general. Among other efforts that aim to improve ultrasound beamforming beyond state of the art, both RF [26] and IQ time-domain implementations [27], [28] have been proposed, but the benefit of using one or the other was unclear. In this work, we have demonstrated a clear benefit to using phase-preserving time-domain implementations, as shown in Figs. 5–12, as opposed to RF data alone and hypothesize that this conclusion would hold true for other approaches. In addition, other groups have demonstrated that their networks are able to generalize to data acquired with

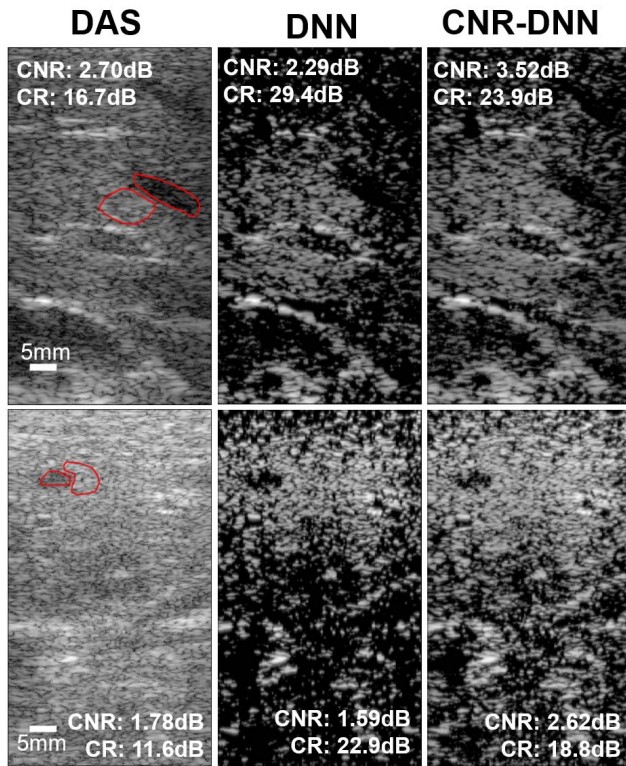


Fig. 14. Qualitative results are shown for experiment 6 (i.e., CNR regularization generalization to *in vivo* data). B-mode images of example *in vivo* liver data beamformed using DAS and DNNs with (right) and without (middle) CNR-regularization. Example regions of interest used to compute image quality metrics are displayed on the DAS images in red. CNR and CR values are indicated on each image. Images are scaled to individual maximums and a 60 -dB dynamic range.

TABLE VI

QUANTITATIVE RESULTS ARE SHOWN FOR EXPERIMENT 6 (I.E., CNR REGULARIZATION GENERALIZATION TO *in vivo* DATA). AVERAGE IMPROVEMENT IN *In Vivo* IMAGE QUALITY METRICS ($n = 15$) COMPARED TO DAS ARE DISPLAYED FOR DNN BEAMFORMING WITH AND WITHOUT CNR REGULARIZATION. STANDARD DEVIATIONS ARE INDICATED IN PARENTHESIS

Metric	DNN	CNR-DNN
CNR (dB)	-0.67 (± 3.31)	0.61 (± 2.95)
CR (dB)	14.7 (± 4.70)	7.80 (± 3.47)
GCNR	0.08 (± 0.15)	0.01 (± 0.16)
SNRs	-0.57 (± 0.29)	-0.33 (± 0.26)

different transducers and imaging parameters [24], [27], but the boundaries and limitations of these generalizations are not well understood. The results in Figs. 7 and 8 support these previous conclusions while also providing insight as to what limitations exist when attempting to generalize to different imaging parameters that were not seen during training. For example, Fig. 7 shows that DNNs are likely robust to frequency changes due to depth-dependent attenuation but, although improvements can persist compared to DAS, we hypothesize that image quality will likely be suboptimal (i.e., smaller and/or more variable improvements in CNR, CR, GCNR, and SNRs compared to DAS) when using a pulse with a substantially lower transmit frequency than what was used during training. Having said that, further studies need to be conducted to test this hypothesis on varied training schemes

and architectures. Finally, in this work, we highlight the challenges associated with selecting network hyperparameters, which is relevant for the field of deep learning in general. These challenges are exacerbated for ultrasound beamforming for which ground-truth training information is difficult to obtain *in vivo*. In this work, we demonstrate that selecting models based on simulation performance can lead to poor performance on *in vivo* data. Although it is possible to use a hold-out *in vivo* validation data set for model selection, it would not address and would likely increase, the discrepancy between training loss and image quality. Therefore, it would be ideal to instead continue to try to tailor training schemes with ground-truth physical information that will result in better translation to *in vivo* performance.

V. CONCLUSION

In this work, we provide a comprehensive comparison and analysis of data representations that can be used for DNN beamforming. Specifically, we compared frequency-domain DNNs to baseband IQ, analytic IQ, and RF time-domain implementations with both single- and multiple-input approaches. Our findings suggest that time-domain and multiple-input implementations are more robust than we previously assumed and, as they are less computationally and architecturally complex, could be better suited for real-time clinical or commercial applications. Moreover, we propose a CNR regularization scheme to improve model selection for *in vivo* beamforming. We demonstrate that CNR regularization addresses the discrepancy we previously encountered between network performance on simulations and *in vivo* data.

ACKNOWLEDGMENT

The authors would like to thank the staff of the Advanced Computing Center for Research and Education (ACCRES), Vanderbilt University, Nashville, TN, USA, for providing computing resources.

REFERENCES

- [1] J. J. Dahl and N. M. Sheth, "Reverberation clutter from subcutaneous tissue layers: Simulation and *in vivo* demonstrations," *Ultrasound Med. Biol.*, vol. 40, no. 4, pp. 714–726, Apr. 2014.
- [2] P.-C. Li and M.-L. Li, "Adaptive imaging using the generalized coherence factor," *IEEE Trans. Ultrason., Ferroelectr., Freq. Control*, vol. 50, no. 2, pp. 128–141, Feb. 2003.
- [3] J. Camacho, M. Parrilla, and C. Fritsch, "Phase coherence imaging," *IEEE Trans. Ultrason., Ferroelectr., Freq. Control*, vol. 56, no. 5, pp. 958–974, May 2009.
- [4] M. A. Lediju, G. E. Trahey, B. C. Byram, and J. J. Dahl, "Short-lag spatial coherence of backscattered echoes: Imaging characteristics," *IEEE Trans. Ultrason., Ferroelectr., Freq. Control*, vol. 58, no. 7, pp. 1377–1388, Jul. 2011.
- [5] J. A. Mann and W. F. Walker, "A constrained adaptive beamformer for medical ultrasound: Initial results," in *Proc. IEEE Ultrason. Symp.*, Oct. 2002, pp. 1807–1810.
- [6] J. F. Synnevag, A. Austeng, and S. Holm, "Adaptive beamforming applied to medical ultrasound imaging," *IEEE Trans. Ultrason., Ferroelectr., Freq. Control*, vol. 54, no. 8, pp. 1606–1613, Aug. 2007.
- [7] I. K. Holfort, F. Gran, and J. A. Jensen, "Broadband minimum variance beamforming for ultrasound imaging," *IEEE Trans. Ultrason., Ferroelectr., Freq. Control*, vol. 56, no. 2, pp. 314–325, Feb. 2009.
- [8] B. Byram and M. Jakovljevic, "Ultrasonic multipath and beamforming clutter reduction: A chirp model approach," *IEEE Trans. Ultrason., Ferroelectr., Freq. Control*, vol. 61, no. 3, pp. 428–440, Mar. 2014.

- [9] B. Byram, K. Dei, J. Tierney, and D. Dumont, "A model and regularization scheme for ultrasonic beamforming clutter reduction," *IEEE Trans. Ultrason., Ferroelectr., Freq. Control*, vol. 62, no. 11, pp. 1913–1927, Nov. 2015.
- [10] K. Dei and B. Byram, "The impact of model-based clutter suppression on cluttered, aberrated wavefronts," *IEEE Trans. Ultrason., Ferroelectr., Freq. Control*, vol. 64, no. 10, pp. 1450–1464, Oct. 2017.
- [11] K. Dei and B. Byram, "A robust method for ultrasound beamforming in the presence of off-axis clutter and sound speed variation," *Ultrasonics*, vol. 89, pp. 34–45, Sep. 2018.
- [12] A. C. Luchies and B. C. Byram, "Deep neural networks for ultrasound beamforming," *IEEE Trans. Med. Imag.*, vol. 37, no. 9, pp. 2010–2021, Sep. 2018.
- [13] D. Perdios, A. Besson, M. Arditi, and J.-P. Thiran, "A deep learning approach to ultrasound image recovery," in *Proc. IEEE Int. Ultrason. Symp. (IUS)*, Sep. 2017, pp. 1–4.
- [14] M. Gasse, F. Millioz, E. Roux, D. Garcia, H. Liebgott, and D. Friboulet, "High-quality plane wave compounding using convolutional neural networks," *IEEE Trans. Ultrason., Ferroelectr., Freq. Control*, vol. 64, no. 10, pp. 1637–1639, Oct. 2017.
- [15] Z. Zhou, Y. Wang, J. Yu, Y. Guo, W. Guo, and Y. Qi, "High spatial-temporal resolution reconstruction of plane-wave ultrasound images with a multichannel multiscale convolutional neural network," *IEEE Trans. Ultrason., Ferroelectr., Freq. Control*, vol. 65, no. 11, pp. 1983–1996, Nov. 2018.
- [16] Y. H. Yoon, S. Khan, J. Huh, and J. C. Ye, "Efficient B-mode ultrasound image reconstruction from sub-sampled RF data using deep learning," *IEEE Trans. Med. Imag.*, vol. 38, no. 2, pp. 325–336, Feb. 2019.
- [17] O. Senouf *et al.*, "High frame-rate cardiac ultrasound imaging with deep learning," in *Proc. Med. Image Comput. Comput. Assist. Intervent.* Cham, Switzerland: Springer, 2018, pp. 126–134.
- [18] S. Khan, J. Huh, and J. Chul Ye, "Universal deep beamformer for variable rate ultrasound imaging," 2019, *arXiv:1901.01706*. [Online]. Available: <http://arxiv.org/abs/1901.01706>
- [19] S. Khan, J. Huh, and J. C. Ye, "Adaptive and compressive beamforming using deep learning for medical ultrasound," *IEEE Trans. Ultrason., Ferroelectr., Freq. Control*, vol. 67, no. 8, pp. 1558–1572, Aug. 2020.
- [20] I. A. M. Huijben, B. S. Veeling, K. Janse, M. Mischi, and R. J. G. van Sloun, "Learning sub-sampling and signal recovery with applications in ultrasound imaging," *IEEE Trans. Med. Imag.*, vol. 39, no. 12, pp. 3955–3966, Dec. 2020.
- [21] N. Kessler and Y. C. Eldar, "Deep-learning based adaptive ultrasound imaging from sub-nyquist channel data," 2020, *arXiv:2008.02628*. [Online]. Available: <http://arxiv.org/abs/2008.02628>
- [22] H. Stroh, S. Rothlübbers, K. Eickel, and M. Günther, "Deep learning-based reconstruction of ultrasound images from raw channel data," *Int. J. Comput. Assist. Radiol. Surgery*, vol. 15, no. 9, pp. 1487–1490, Sep. 2020.
- [23] W. Simson *et al.*, "End-to-end learning-based ultrasound reconstruction," 2019, *arXiv:1904.04696*. [Online]. Available: <http://arxiv.org/abs/1904.04696>
- [24] A. Wiacek, E. Gonzalez, and M. A. L. Bell, "CohereNet: A deep learning architecture for ultrasound spatial correlation estimation and coherence-based beamforming," *IEEE Trans. Ultrason., Ferroelectr., Freq. Control*, vol. 67, no. 12, pp. 2574–2583, Dec. 2020.
- [25] A. A. Nair, T. D. Tran, A. Reiter, and M. A. Lediju Bell, "A deep learning based alternative to beamforming ultrasound images," in *Proc. IEEE Int. Conf. Acoust., Speech Signal Process. (ICASSP)*, Apr. 2018, pp. 3359–3363.
- [26] A. A. Nair, T. D. Tran, A. Reiter, and M. A. L. Bell, "A generative adversarial neural network for beamforming ultrasound images : Invited presentation," in *Proc. 53rd Annu. Conf. Inf. Sci. Syst. (CISS)*, Mar. 2019, pp. 1–6.
- [27] A. A. Nair, K. N. Washington, T. D. Tran, A. Reiter, and M. A. Lediju Bell, "Deep learning to obtain simultaneous image and segmentation outputs from a single input of raw ultrasound channel data," *IEEE Trans. Ultrason., Ferroelectr., Freq. Control*, vol. 67, no. 12, pp. 2493–2509, Dec. 2020.
- [28] D. Hyun, L. L. Brickson, K. T. Looby, and J. J. Dahl, "Beamforming and speckle reduction using neural networks," *IEEE Trans. Ultrason., Ferroelectr., Freq. Control*, vol. 66, no. 5, pp. 898–910, May 2019.
- [29] A. C. Luchies and B. C. Byram, "Training improvements for ultrasound beamforming with deep neural networks," *Phys. Med. Biol.*, vol. 64, no. 4, Feb. 2019, Art. no. 045018.
- [30] R. Zhuang and J. Chen, "Deep learning based minimum variance beamforming for ultrasound imaging," in *Smart Ultrasound Imaging and Perinatal, Preterm and Paediatric Image Analysis*. Cham, Switzerland: Springer, 2019, pp. 83–91.
- [31] A. C. Luchies and B. C. Byram, "Assessing the robustness of frequency-domain ultrasound beamforming using deep neural networks," *IEEE Trans. Ultrason., Ferroelectr., Freq. Control*, vol. 67, no. 11, pp. 2321–2335, Nov. 2020.
- [32] K. Hornik, M. Stinchcombe, and H. White, "Multilayer feedforward networks are universal approximators," *Neural Netw.*, vol. 2, no. 5, pp. 359–366, Jan. 1989.
- [33] M. Bianchini and F. Scarselli, "On the complexity of neural network classifiers: A comparison between shallow and deep architectures," *IEEE Trans. Neural Netw. Learn. Syst.*, vol. 25, no. 8, pp. 1553–1565, Aug. 2014.
- [34] E. Vienneau, A. Luchies, and B. Byram, "An improved training scheme for deep neural network ultrasound beamforming," in *Proc. IEEE Int. Ultrason. Symp. (IUS)*, Oct. 2019, pp. 568–570.
- [35] A. A. Nair, M. R. Gubbi, T. D. Tran, A. Reiter, and M. A. L. Bell, "A fully convolutional neural network for beamforming ultrasound images," in *Proc. IEEE Int. Ultrason. Symp. (IUS)*, Oct. 2018, pp. 1–4.
- [36] A. A. Nair, T. D. Tran, A. Reiter, and M. A. Lediju Bell, "One-step deep learning approach to ultrasound image formation and image segmentation with a fully convolutional neural network," in *Proc. IEEE Int. Ultrason. Symp. (IUS)*, Oct. 2019, pp. 1481–1484.
- [37] T. Glasmachers, "Limits of end-to-end learning," 2017, *arXiv:1704.08305*. [Online]. Available: <http://arxiv.org/abs/1704.08305>
- [38] R. Mallart and M. Fink, "The van Cittert–Zernike theorem in pulse echo measurements," *J. Acoust. Soc. Amer.*, vol. 90, no. 5, pp. 2718–2727, Nov. 1991.
- [39] A. Paszke *et al.*, "Automatic differentiation in pytorch," in *Proc. 31st Conf. Neural Inf. Process. Syst. (NIPS)*, Long Beach, CA, USA, 2017.
- [40] X. Glorot, A. Bordes, and Y. Bengio, "Deep sparse rectifier neural networks," in *Proc. 14th Int. Conf. Artif. Intell. Statist.*, 2011, pp. 315–323.
- [41] D. P. Kingma and J. Ba, "Adam: A method for stochastic optimization," 2014, *arXiv:1412.6980*. [Online]. Available: <http://arxiv.org/abs/1412.6980>
- [42] X. Glorot and Y. Bengio, "Understanding the difficulty of training deep feedforward neural networks," in *Proc. 13th Int. Conf. Artif. Intell. Statist.*, 2010, pp. 249–256.
- [43] K. He, X. Zhang, S. Ren, and J. Sun, "Delving deep into rectifiers: Surpassing human-level performance on ImageNet classification," in *Proc. IEEE Int. Conf. Comput. Vis. (ICCV)*, Dec. 2015, pp. 1026–1034.
- [44] R. F. Wagner, S. W. Smith, J. M. Sandrik, and H. Lopez, "Statistics of speckle in ultrasound B-scans," *IEEE Trans. Sonics Ultrason.*, vol. 30, no. 3, pp. 156–163, May 1983.
- [45] J. A. Jensen, "FIELD: A program for simulating ultrasound systems," in *Proc. IEEE 10th Nordic-Baltic Conf. Biomed. Imag.*, vol. 34, Mar. 1996, pp. 351–353.
- [46] R. Demirli and J. Saniie, "Asymmetric Gaussian chirplet model for ultrasonic echo analysis," in *Proc. IEEE Int. Ultrason. Symp.*, Oct. 2010, pp. 124–128.
- [47] A. Rodriguez-Molares *et al.*, "The generalized contrast-to-noise ratio: A formal definition for lesion detectability," *IEEE Trans. Ultrason., Ferroelectr., Freq. Control*, vol. 67, no. 4, pp. 745–759, Apr. 2020.
- [48] S. W. Smith, R. F. Wagner, J. M. Sandrik, and H. Lopez, "Low contrast detectability and contrast/detail analysis in medical ultrasound," *IEEE Trans. Sonics Ultrason.*, vol. 30, no. 3, pp. 164–173, May 1983.



Jaime Tierney received the B.A. degree in mathematics from the College of the Holy Cross, Worcester, MA, USA, in 2012, and the Ph.D. degree in biomedical engineering from Vanderbilt University, Nashville, TN, USA, in 2019.

She worked for two years as an Image Analyst at inviCRO, Boston, MA, USA, a medical imaging services and software company. She is currently a Postdoctoral Fellow with the Data Science Institute, Vanderbilt University. Her current research interests include machine learning methods for

ultrasound beamforming and slow blood flow ultrasound imaging without contrast.



Adam Luchies received the B.Sc. degree in Engineering from John Brown University, Siloam Springs, AR, USA, in 2009, and the M.S. and Ph.D. degrees in electrical and computer engineering from the University of Illinois at Urbana-Champaign, Champaign, IL, USA, in 2011 and 2016, respectively, under the mentorship of Michael Oelze. He completed his postdoctoral training at Vanderbilt University under the mentorship of Brett Byram.

He is currently an Ultrasound Engineer at Siemens Health Care, Issaquah, WA, USA.



Matthew Berger received the B.S. and M.S. degrees in computer science from Binghamton University, Binghamton, NY, USA, in 2005 and 2007, respectively, and the Ph.D. degree in computing from The University of Utah, Salt Lake City, UT, USA, in 2013.

He is currently an Assistant Professor with the Department of Computer Science and Electrical Engineering, Vanderbilt University, Nashville, TN, USA. He was a Postdoctoral Research Associate with The University of Arizona, Tucson, AZ, USA. His research interests are in data visualization and machine learning.



Brett Byram (Member, IEEE) received the B.S. degree in biomedical engineering and math from Vanderbilt University, Nashville, TN, USA, in 2004, and the Ph.D. degree in biomedical engineering from Duke University, Durham, NC, USA, in 2011.

He was a Research Assistant Professor with Duke University. In 2013, he joined the Biomedical Engineering Department, Vanderbilt University, Nashville, TN, USA, as an Assistant Professor. He has spent time working at the Center for Fast Ultrasound, Jørgen Jensen, Kongens Lyngby, Denmark, and the Ultrasound Division, Siemens Healthcare, Mountain View, CA, USA. He currently runs the Biomedical Elasticity and Acoustic Measurement (BEAM) Laboratory, where he and others in the lab pursue solutions to clinical problems using ultrasound. He is also with the Vanderbilt Institute for Surgery and Engineering (VISE) and the Vanderbilt University Institute of Imaging Science (VUIIS). His research interests include beamforming, motion estimation, and other related signal processing and hardware development tasks.